

Atomistic mechanisms underlying the maximum in diffusivity in doped $\text{Li}_7\text{La}_3\text{Zr}_2\text{O}_{12}$

Juan C. Verduzco, Ernesto E. Marinero, and Alejandro Strachan*

*Corresponding author:

Alejandro Strachan (strachan@purdue.edu)

Phone: +1 765 496 3551

Fax: +1 765 494 1204

School of Materials Engineering and Birck Nanotechnology Center
Purdue University, West Lafayette, Indiana, 47907 USA

Abstract

Doped lithium lanthanum zirconium oxide (LLZO) is a promising class of solid electrolytes for lithium-ion batteries due to their good electrochemical stability and compatibility with Li metal anodes. Ionic diffusivity in these ceramics is known to occur via correlated, vacancy mediated, jumps of Li^+ between alternating tetrahedral and octahedral sites. Aliovalent doping at the Zr-site increases the concentration of vacancies in the Li^+ sublattice and cation diffusivity, but such an increase is universally followed by a decrease for Li^+ concentration lower than 6.3 - 6.5 Li molar content. Molecular dynamics simulations based on density functional theory show that the maximum in diffusivity originates from competing effects between the increased vacancy concentration and the increasing occupancy of the low-energy tetrahedral sites by Li^+ , which increases the overall activation energy associated with diffusion. For the relatively high temperatures of our simulations, Li^+ concentration plays a dominant role in transport as compared to dopant chemistry.

1 Introduction

Lithium batteries with high energy density, improved safety, and faster charging rates are instrumental in meeting the energy demands for electric vehicles¹, advanced wearable and portable devices², and renewable energy storage systems³. Conventional liquid electrolyte based batteries cannot satisfy these requirements, as they are incompatible with high-energy anode materials and fall short in key safety features⁴. Replacing organic liquid electrolytes with solid electrolytes in these systems is expected to improve mechanical properties, minimize safety risks due to improved thermal and electrochemical stability, and enable the pairing with high-energy-density anodes to improve battery capacity. However, practical applications for solid-state batteries are limited, as liquid chemistries generally surpass solid electrolytes in important metrics such as interfacial resistance and ionic conductivity^{4,5}.

Lithium lanthanum zirconium oxide ($\text{Li}_7\text{La}_3\text{Zr}_2\text{O}_{12}$, LLZO) ceramic garnet has emerged as a prominent and promising candidate for all-solid-state battery applications⁶. Aliovalent dopants provide an important avenue for the optimizing its transport properties⁷. In LLZO, lithium ions occupy alternating tetrahedral (24d) and a distorted octahedral (96h) sites forming 3D channels for ionic diffusion. As is often the case in solid-state diffusion, transport in the Li+ sublattice is mediated by vacancies⁸. LLZO exhibits room temperature ionic conductivity of approximately 1×10^{-4} S/cm⁶, while doped LLZO has been reported to reach roughly 1.8×10^{-3} S/cm for a dual-substituted Ga/Sc ceramic⁹.

Substitutional dopants have multiple effects on LLZO, and several mechanisms have been proposed to explain the role of doping on its ionic conductivity. Doping affects the relative stability between two polymorphs and stabilization of the cubic polymorph, which has ionic conductivity two orders of magnitude higher than the tetragonal phase, is critical^{10;11}. However, doping has additional effects and can significantly influence transport within the cubic phase. Aliovalent dopants alter the occupancy of the Li-sublattice since charge compensation mainly occurs through the introduction of Li vacancies¹². The increase in vacancies accelerates diffusion but reduces the number of carriers in the sublattice. Dopants also alter the local chemistry experienced by the mobile Li+ ions during diffusion. Changes in the 3D channels of Li-sublattice can introduce bottlenecks that alter Li migration pathways¹³. Experimental results across different dopants show that while the detailed chemistry affects transport, a general trend emerges of increasing conductivity with decreasing Li+ content for weak doping, followed by a maximum between 6.3 – 6.5 Li molar content, and a subsequent reduction^{11;14;15;16}.

To elucidate the mechanisms responsible for the experimental observations, several computational studies have utilized electronic structure calculations to investigate transport in tetragonal and cubic LLZO^{17;18} as well as the energetics of doping and its effect on transport^{19;20;21}. Dopants can occupy various sites in the LLZO structure. Miara et al. calculated defect energies to map the site and oxidation state preference for a broad range of elements, demonstrating the potential for many stable doped LLZO structures²².

Molecular dynamics (MD) simulations based on density functional theory (DFT) have demonstrated that correlated motions of Li ions are a key mechanism behind the superionic conductivity of cubic LLZO ceramics¹⁹. These simulations have revealed that transport within the Li+ sublattice is not dominated by independent hops between alternating sites, but by multiple ions experiencing collective transitions (correlated in time and space)²³. In contrast, Meier et al.¹⁸ suggest mechanisms characterized by asynchronous jumps in cubic LLZO, while Chen et al.²³ found that diffusion in cubic LLZO is hindered by back-and-forth jumps, originating from the low concentration of vacancies in LLZO. Monte Carlo simulations on the garnet lattice provided insight and established general trends on the effect of Li+ concentration, the relative energy between sites, and short range interactions on transport²⁴, but do not capture specific chemical effects or long range electrostatic interactions important in the cases of interest here. Thus, important questions regarding the underlying transport mechanisms in LLZO and crucially, the observed maximum in ionic diffusivity vs. Li+ concentration observed across dopants, remains unexplained.

In this paper, we analyze how changes in Li+ concentration, resulting from aliovalent substitution and by artificially removing Li atoms in the simulation, affect the population of octahedral (O) sites and tetrahedral (T) sites, associated residence times, and correlations between the various individual Li+ jumps. We find that the maximum diffusivity with decreasing Li+ originates from the competition between increasing vacancies that accelerates transport and the increasing occupancy of low-energy T sites that results in an increase in the overall activation energy for diffusion. Furthermore, our simulations, at temperatures above 1200K, show correlated hops within timescales

of a picosecond. These correlations decrease with decreasing temperature, and reveal how doping influences correlated jumps.

2 Computational Details

MD simulations were executed using Kohn-Sham DFT as implemented in the Vienna Ab-initio Simulation Package (VASP)^{25;26}. The chosen kinetic energy cutoff is a compromise between accuracy and computational expedience, given the large number of MD simulations required to explore chemistry and compositional space. The simulations reported in this paper required over 1.7 million core hours of computing. To verify the accuracy of the results, we conducted two additional simulations using a kinetic energy cutoff of 500 eV and can confirm both qualitative and quantitative agreement with the results with the smaller basis set. The exchange and correlation functional were described within the generalized gradient approximation using PBEsol²⁷, which improves the Perdew-Burke-Ernzernhof (PBE)²⁸ functional for solids. We used projector augmented wave (PAW) pseudopotentials to describe core electrons²⁹. No spin polarization was considered.

The crystal structure for cubic LLZO with formula $Li_{56}La_{24}Zr_{16}O_{96}$ ³⁰ was obtained from the Inorganic Crystal Structure Database (ICSD)³¹. To generate Bi-doped and Ta-doped structures, we stochastically replaced the desired number of Zr atoms with Bi/Ta. Compositions analyzed were created with substitutions in the formula $Li_{56-x}La_{24}Zr_{16-x}O_{96}$ for $x = (4, 6, 8)$ to mirror compositions $Li_{7-x}La_3Zr_{2-x}M_xO_{12}$. Substitution of the Zr 16a site by Bi and Ta has been reported in prior experiments^{32;15;33}. Due to the supervalent substitution, one lithium atom is removed per Bi or Ta, to account for the change in oxidation state from Zr (4+) to Tantalum/Bismuth (5+). We studied compositions between Li molar contents, x_{Li} , 0 and 1 $Li_{7-x}La_3Zr_{2-x}M_xO_{12}$ for $x = (0, 0.5, 0.75, 1)$, resulting in a range of overall occupancy of the Li+ sublattice from 48/72 to 56/72. To separate the role of chemistry and the change in Li lattice occupancy on transport, we performed simulations on structures where Li+ cations were removed without the substitutional doping. Since all these relatively small systems can be influenced by the different atomistic configurations resulting from aliovalent substitutions, each structure was independently generated with stochastic replacements, thus exploring distinct arrangements of the local environments. Lattice parameters were taken from room temperature experimental measurements for pure LLZO, Bi-doped LLZO³², and Ta-doped LLZO³⁴ as shown in Table 1.

As mentioned previously, the Li sublattice consists of two types of sites: 24d T sites and 96h O sites. The latter comprises closely located pairs, and previous studies have shown that two lithium atoms cannot simultaneously occupy these split 96h sites²⁰. This effectively leaves us with only 48 possible O spaces for ion diffusion. Given that tetrahedral sites are known to be energetically favorable in similar structures^{35;36}, we initially distributed the Li atoms to occupy all the tetrahedral sites, with the remaining atoms randomly placed on the octahedral split sites 96h, ensuring that no consecutive split sites were simultaneously occupied. During the MD equilibration of the structures, atoms migrated from this initial configuration to preferentially occupy the O sites, driven by the minimization of electrostatic repulsion between Li+ ions, in good agreement with prior work.

We performed isochoric and isothermal MD simulations at $T = 1273$ K and $T = 1773$ K with a 1 fs timestep. These temperatures were selected to capture diffusive behavior at timescales achievable with DFT-based MD. All molecular dynamics simulations ran for between 40 and 60 ps, long enough to achieve the diffusive regime and extract a diffusion constant, as demonstrated by the MSD plots in Fig. S1. A Nosé-Hoover thermostat was used to sample the canonical ensemble with a mass corresponding to a period of 40fs. We note that due to the random nature of the doping, the results can be affected by the specific configuration created. Each structure was independently and

Table 1 Experimental lattice parameters for doped LLZO structures.

STRUCTURE	LATTICE PARAMETER	NUMBER OF ATOMS	NUMBER OF LITHIUM ATOMS
LLZO	12.994 Å	192	56
LLZO (Bi = 0.5)	13.019 Å	188	52
LLZO (Bi = 0.75)	13.031 Å	186	50
LLZO (Bi = 1)	13.045 Å	184	48
LLZO (Ta = 0.5)	12.919 Å	188	52
LLZO (Ta = 0.75)	12.904 Å	186	50
LLZO (Ta = 1)	12.890 Å	184	40
LLZO (LiV = 0.5)	12.994 Å	188	52
LLZO (LiV = 0.75)	12.994 Å	186	50
LLZO (LiV = 1)	12.994 Å	184	48
LLZO (LiV = 1.25)	12.994 Å	182	46

stochastically generated, allowing us to assess the effects of atomic structure and other simulation details on transport and other properties by exploring trends across chemistries and compositions. As with all physics-based modeling, our simulations are not without approximations. We did not include relativistic effects, which could play a role in our systems (especially those with Bi), for consistency across the various chemistries and to keep computational resources manageable. In addition, we artificially maintained the neutrality of the system with artificial vacancies (i.e. we removed Li atoms not Li+). The motivation behind this choice is the challenge associated with the presence of several localized charges in cells with periodic boundary conditions. These approximations are justified a posteriori by our finding of similar overall trends in terms of diffusivity and site occupancy between Ta and Bi doping and the case with artificial vacancies. Future work to explore the effect of these assumptions would be of interest.

3 Results & Discussion

3.1 Diffusivity vs. Li+ concentration

To compute the diffusion constant of Li+, we calculated the mean squared displacement ($\langle R^2 \rangle$) of Li+ as a function of time (see SI, Fig. S1) and fitted the linear section (after a diffusive regime is achieved) to the expression $\langle R^2 \rangle = 3Dt$. Fig. 1(a) shows the diffusion coefficient obtained from our MD simulations as a function of lithium content (dopant quantity on the top axis) for both temperatures and the two dopants studied, as well as the models with artificially modified Li contents. Interestingly, our results suggest that the occupancy of the Li sublattice has a more significant influence on Li+ transport than the specific chemistry of the dopant.

At $T = 1773$ K, we find a monotonic increase in diffusivity with decreasing Li+ content for all materials studied. Quite interestingly, at $T = 1273$ K, we observe an initial increase in conductivity with doping, a maximum at an intermediate Li+ concentration of approximately 6.5, followed by either a reduction or plateau. This is consistent with a maximum in ionic conductivity for a Li+ molar content of approximately 6.5 observed experimentally at lower temperatures^{11;14;16}. We attribute deviations from these general trends to the small sample sizes and short simulation times

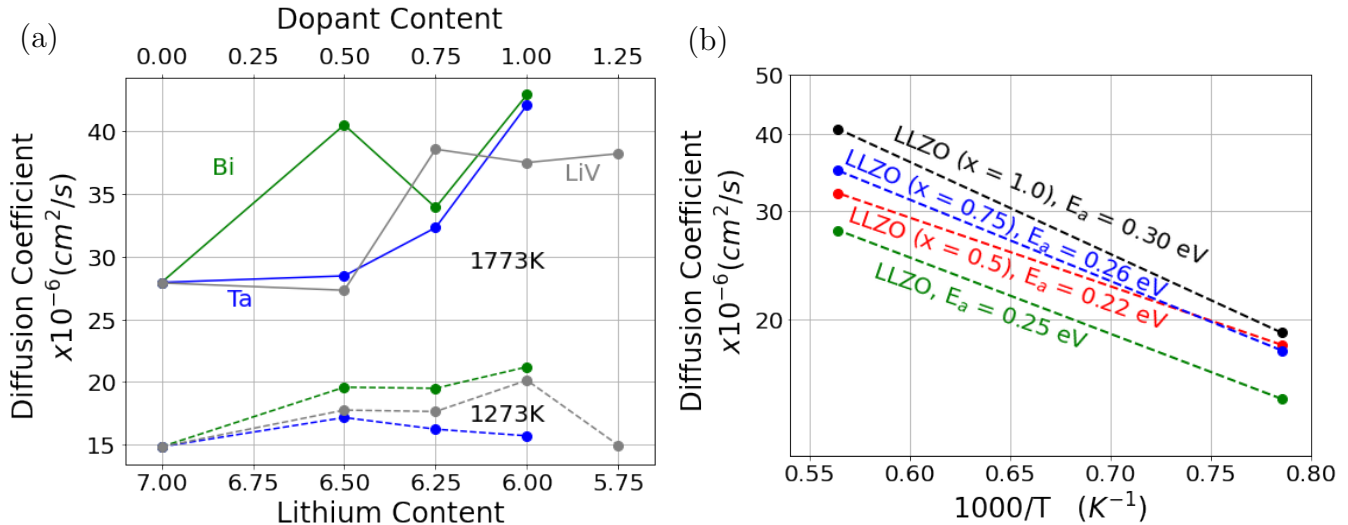


Figure 1 (a) Diffusion coefficients versus Lithium content. Colors represent different dopants, and LiV represents a structure created with artificial vacancies. (b) Diffusion coefficients versus inverse temperature. Colors indicate different dopant contents.

intrinsic to the DFT-MD simulations. Accurate interatomic potentials for these systems, including dopants, would enable simulations of larger systems and longer timescales, which would reduce the noise in the diffusivity results. Fig. 1(b) shows an Arrhenius plot of the resulting diffusion coefficients and estimates of the effective activation energies. These activation energies are rough estimates and are computed to confirm independent observations regarding the mechanisms behind the maximum in conductivity. The remainder of the paper analyzes the mechanisms behind the trends observed in Fig. 1.

The Li+ sublattice consists of 24 tetrahedral sites and 48 split-octahedral sites, and transport occurs via alternating jumps between tetrahedral and octahedral sites^{19;37}. To understand the trends in diffusivity discussed above, we performed a detailed analysis of the MD trajectories, tracking the time evolution of individual Li+ ions. This was done by mapping each ion onto a sublattice site using a distance-based criterion and recording each jump. Fig. 2 shows the average occupancy of the O and T sites, n_O and n_T , as a function of Li+ content. Confidence intervals (95%) for these values are estimated at 0.003 for tetrahedral occupancy and 0.001 for octahedral occupancy. As noted in prior work^{18;36}, in LLZO the Li+ ions preferentially occupy the more populous, but higher energy, O sites to minimize electrostatic repulsion. A reduction of the Li+ concentration (either by doping or artificially) from the LLZO value results in an initial reduction in both n_O and n_T . However, for Li+ molar contents below 6.5, the population of the low-energy T sites actually increases at the expense of O sites³⁷. These observations apply regardless of temperature and dopant chemistry. As discussed in Section 2, we performed two additional simulations with a more complete basis set. They correspond to stoichiometric LLZO and LLZO (LiV = 1.25). After 25 ps of DFT-MD, the values for site occupancy are within 5% of those reported in Fig. 2 and the residence times are within 15%. The increase in n_T with decreasing Li+ content might appear counterintuitive at first sight, but it is the result of the reduced importance of electrostatic repulsion (which drives the ions to the O sites in pure LLZO), with ions preferring the low-energy T sites. We note that Monte Carlo simulations²⁴ including short-range interactions do not capture the minimum in occupancy of the T sites in the range of interest for doped LLZO observed here.

Having established where Li+ ions are located as a function of Li+ molar content, we now

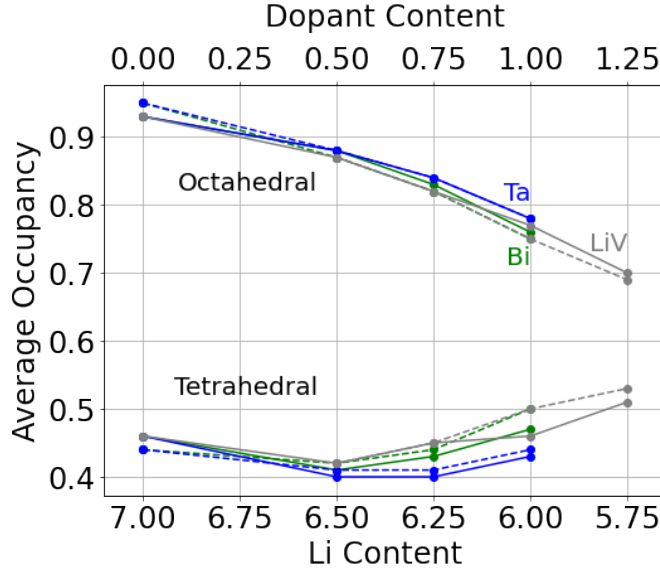


Figure 2 Site-wise occupancy of different doped-LLZO structures from MD simulations. Colors represent different dopants, and LiV represents a structure created with artificial vacancies. Dashed lines represent $T=1273$ K and solid lines $T=1773$ K. The two groups of lines describe the two independent sites in the Li sublattice.

focus on the jumps between neighboring sites. Since the network topology forces ions to move by alternating between O and T sites, the number of $T \rightarrow O$ and $O \rightarrow T$ jumps over time tend to the same value and are nearly identical in our simulations (see SI, Fig. S1). Thus, the average residence times, τ_O and τ_T , of the Li^+ atoms in O and T sites respectively, are related to the occupancies according to:

$$\frac{24 * n_T}{\tau_T} = \frac{48 * n_O}{\tau_O} \quad (1)$$

where the coefficients 24 and 48 represent the number of T and O sites in the unit cell, respectively. We note that transitions between octahedral sites (96h) that bypass the tetrahedral site have been reported for garnets with lower Li contents³⁸. However, such processes were not observed in our study, which is consistent with previous reports^{8;19;39}.

The computed average residence times in O and T sites are shown as a function of Li content in Fig. 3. As expected from Eq. 1, the residence times in O sites are longer than those for T sites. Jumping statistics reveal a Poisson-like diffusion behavior for these systems, in agreement with previous reports for undoped cubic LLZO garnets²³. Representative residence time distributions and confidence intervals (95%) calculated from our analysis are included as Fig. S3 and Table S2. At $T = 1773$ K, the residence time in O sites decreases monotonically with decreasing Li^+ concentration, while the residence time in T sites follows a similar trend for low doping but levels off for Li^+ molar content below 6.5. This plateau is due to the increase in occupancy of T sites (n_T) as shown in Fig. 2. Faster diffusion and shorter residence times are expected since reducing the Li^+ concentration increases the number of vacant sites and the number of available jumps at any given time. At $T = 1273$ K, we observe similar trends for Li^+ concentrations near the LLZO values. However, remarkably, as x_{Li} decreases below approximately 6.5, the residence time for the O sites plateaus and that for T sites increases quite sharply. This is associated with the maximum in diffusion coefficient and its subsequent decline with doping for Li^+ molar contents below 6.5.

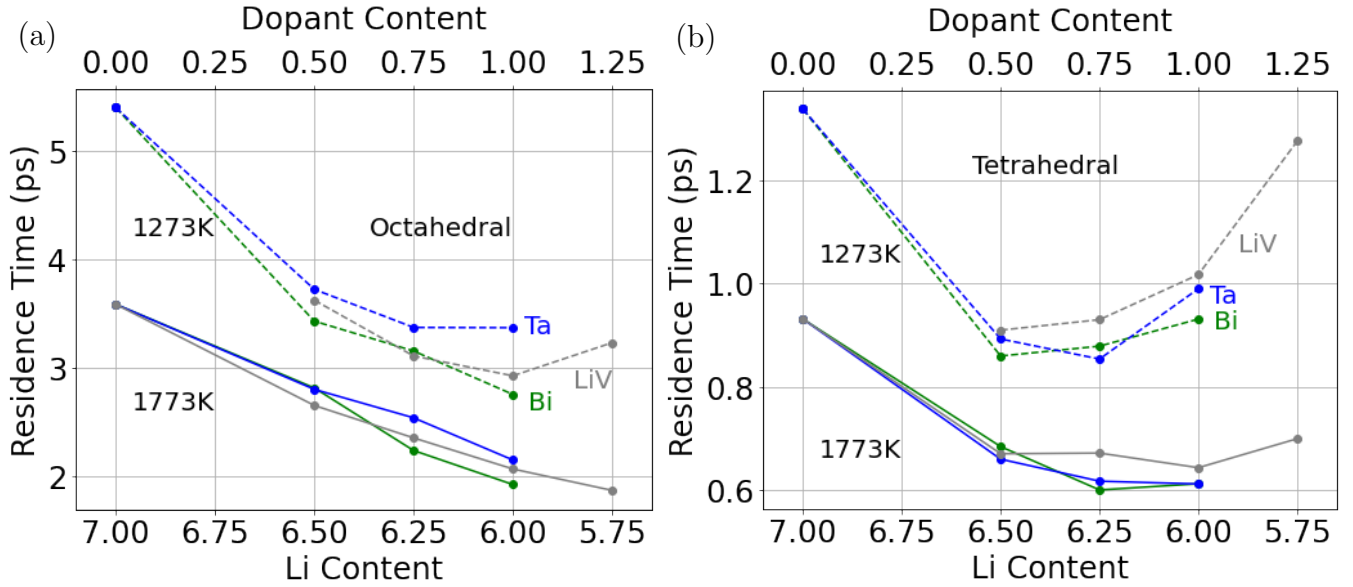


Figure 3 Average residence time of different doped-LLZO structures from MD simulations against the stoichiometric Li molar content, (a) for O sites and (b) for T sites.

The relative values of τ_O and τ_T are a direct consequence of the increasing occupation of T sites and Eq. 1, but the trend in absolute residence times observed at 1273 K, which correlates with the observed maximum in diffusivity, is more subtle. The initial decrease in residence times is due to the increase in the density of vacancies. The increase in residence time and decrease in diffusion coefficient at $T = 1273\text{K}$ for x_{Li} below approximately 6.5 can be understood by recalling that the T sites are lower in energy than the O sites for Li^+ . Thus, the topologically-required increase in the fraction of $\text{T} \rightarrow \text{O}$ jumps with increasing population of (low energy) T sites results in a higher overall activation energy for diffusion. Our MD results confirm this picture. An effective activation energy can be estimated from the Arrhenius plots in Fig. 1(b) that indicate a lower activation energy for $\text{Li}_{7-x}\text{La}_3\text{Zr}_{2-x}\text{M}_x\text{O}_{12}$ with $x = 0.5$.

3.2 Correlated Events and Li^+ transport

The residence times discussed above capture the overall trends of diffusivity vs. composition but do not account for the correlation between neighboring events, which has been shown to play an important role in ionic transport in LLZO^{18;23}. This section quantifies the percentage of return jumps, when two subsequent jumps leave an ion in its original site, and time correlations between neighboring events. Taking advantage of the clearly defined 3D channels of the LLZO structure, and the alternating pattern of T and O sites, we computed the fraction of ions jumping back to their original site after a transition. An ideal random walk in the Li^+ sublattice would have a return probability of 50% for $\text{T} \rightarrow \text{O} \rightarrow \text{T}$ (since each O site is connected to two T sites) and 25% for $\text{O} \rightarrow \text{T} \rightarrow \text{O}$ transitions. Fig. 4 shows return probabilities as a function of Li^+ concentration for the various cases studied. To quantify the uncertainty of these probabilities, an ensemble approach subdividing the simulation shows an average deviation from the mean of ± 0.025 . As with other transport characteristics, chemistry plays a minor role as compared with Li^+ concentration for the conditions studied. We find that the return probability following a $\text{T} \rightarrow \text{O}$ jump ranges from 0.25 to 0.35, significantly below the random value, indicating a higher than random chance of moving

forward. The simulations reveal an overall trend towards the random value with decreasing Li+ content at $T = 1273$ K and little change at $T = 1773$ K. In the case of $O \rightarrow T$ transitions, we also observe an increase in return fractions with doping at the lower temperature and flat value at 1773 K, but the numbers are closer to the random case (actually, our results show values over 0.25 for the low temperature and smallest Li+ concentrations).

The return probabilities are consistent with prior results indicating concerted migration^{19;21;23;36} where several atoms move nearly simultaneously. As will be shown below, vacating a T site often results in nearly instantaneous occupation by a neighboring Li+, preventing a return. The observation of return probabilities closer to the random value for $O \rightarrow T$ can be attributed to the lower average occupancy of the T site, which reduces the probability of a neighboring Li+ occupying the vacated O site. Our results differ from those in Ref.²³, which reported significant return jumps attributed to low vacancy concentrations. The origin of this difference is unclear at this point; it could be due the fact that our work uses DFT simulations and Chen et al. use a force field or differences in the analysis. We note that less-than-random return probabilities are consistent with the widely accepted correlated hops involving multiple ions.

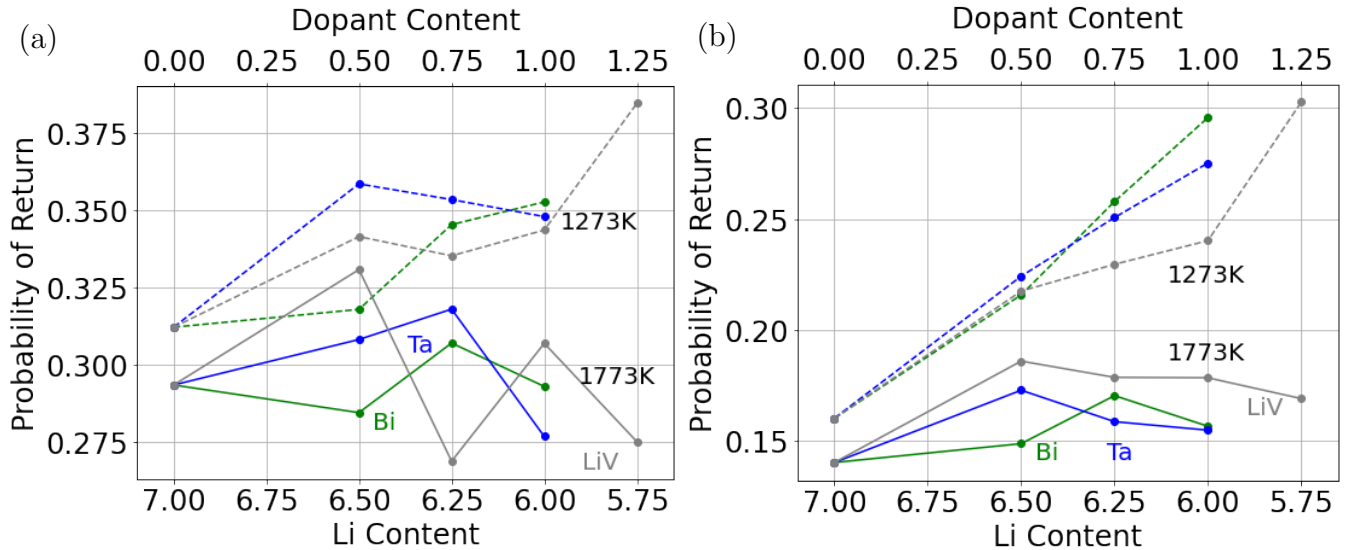


Figure 4 Return probabilities for doped-LLZO structures from MD simulations against the stoichiometric Li molar content, (a) for $T \rightarrow O \rightarrow T$ jumps, and (b) $O \rightarrow T \rightarrow O$ jumps. Colors represent different dopants, and LiV represents a structure created with artificial vacancies. Dashed lines represent $T=1273$ K and solid lines $T=1773$ K.

To gain additional insight into correlated jumps, we characterized time correlations between jumps in neighboring sites. We computed the distribution of times between several pair of events, labeled from 1 to 16, see Fig. 5. The first event, which can be a $T \rightarrow O$ transition (Fig. 5(a)) or a $O \rightarrow T$ (Fig. 5(b)) transition is shown as a black arrow and marked with a star. The second event could involve the same Li+ (black arrows) or a different ion (color arrow). The number next to the arrow labels the event (see also Table 2 in the SI). We define time correlation functions between two events, E_1 at time t_1 and E_2 at time t_2 as:

$$C_{E_1 E_2}(t) = \frac{n_{E_1 E_2}(t, \Delta)}{N_{E_1} \cdot n_{E_2 | E_1}(\Delta)} \quad (2)$$

where the numerator represents the number of E_2 events following a E_1 event after a time between

t and $t + \Delta$ normalized by Δ . The denominator is a normalization factor obtained as the product of number of E_1 times the average rate of event E_2 given the configuration resulting from E_1 .

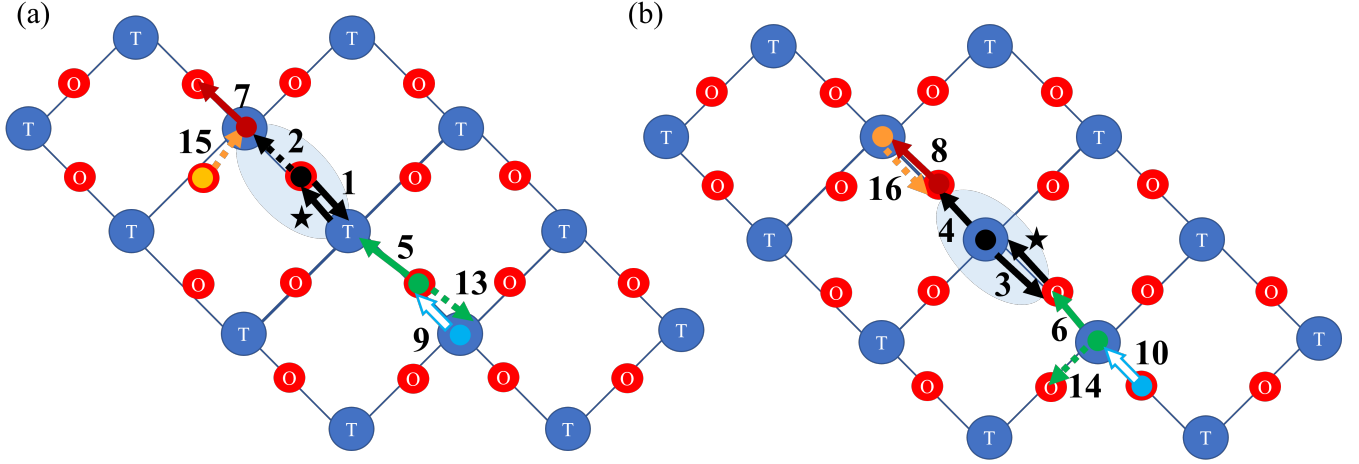


Figure 5 Schematic representation of possible secondary events to study correlated transitions. Initial jumps are marked with a (★). Colors represent different Li atoms occupying different sites. Arrows represent the rate of secondary transitions, with dashed lines being anticorrelated events. Arrows representing multiplicity of events were omitted for clarity. (a) shows Cases with an initial event as T→O and (b) O→T

Table 2 Summary of pair-wise correlated mechanisms studied. T1 and T2 represent the first and second tetrahedral sites involved. O1 and O2 represent the first and second octahedral sites involved.

CASE	SAME LI	FIRST EVENT	SECOND EVENT	COMMENT	MULTIPLICITY
1	YES	T1→O1	O1→T1		
2	YES	T1→O1	O1→T2		
3	YES	O1→T1	T1→O1		
4	YES	O1→T1	T1→O2		
5	NO	T1→O1	O2→T1		3
6	NO	O1→T1	T2→O1		1
7	NO	T1→O1	T2→O2	O1 + T2 (1st NN) ^a	3
8	NO	O1→T1	O2→T2	T1 + O2 (1st NN)	3
9	NO	T1→O1	T2→O2	T1 + O2 (1st NN)	3
10	NO	O1→T1	O2→T2	O1 + T2 (1st NN)	3
13	NO	T1→O1	O2→T2	T1 + O2 (1st NN)	3
14	NO	O1→T1	T2→O2	O1 + T2 (1st NN)	3
15	NO	T1→O1	O2→T2	O1 + T2 (1st NN)	3
16	NO	O1→T1	T2→O2	T1 + O2 (1st NN)	3

^a1st NN indicates first nearest neighbors in the sublattice.

Fig. 6 shows the time correlations for key pairs of jumps for Bi-doped LLZO. Plots for the lower temperature time correlations are included as Fig. S2. Case numbers follow those in our analysis

scripts shared on Github⁴⁰. Cases 11 and 12 are not shown because they involve 3 Li atoms. The event pairs shown in the top row exhibit short-time correlations, i.e. E_2 is more likely to occur soon after E_1 while in the cases shown in the second row event E_1 inhibits E_2 . In all cases, time correlations are negligible beyond 1 ps, with this correlation time being consistent with results in Ref.²³. As expected, in some cases, reducing Li+ concentration reduces correlations. The strongest short-range correlation observed is case 6, where a vacated O site is filled from a neighboring T site. Interestingly, the related process associated with a vacated T site shows a much weaker time correlation. We attribute this to the electrostatic repulsion that tends to maximize the occupancy of O sites. Not surprisingly, the short-time correlation in case 6 weakens drastically with the reduction in Li+ content. Cases 13 and 14, which track the opposite transitions of Cases 5 and 6, where the second atom does not follow the initial jump, are anticorrelated at short times. Cases 7 and 8 describe time correlated motions where a site is vacated followed by a first-neighboring site being occupied (due to the reduction in electrostatic repulsion) and Cases 15 and 16 show, conversely, that the opposite motion is hindered.

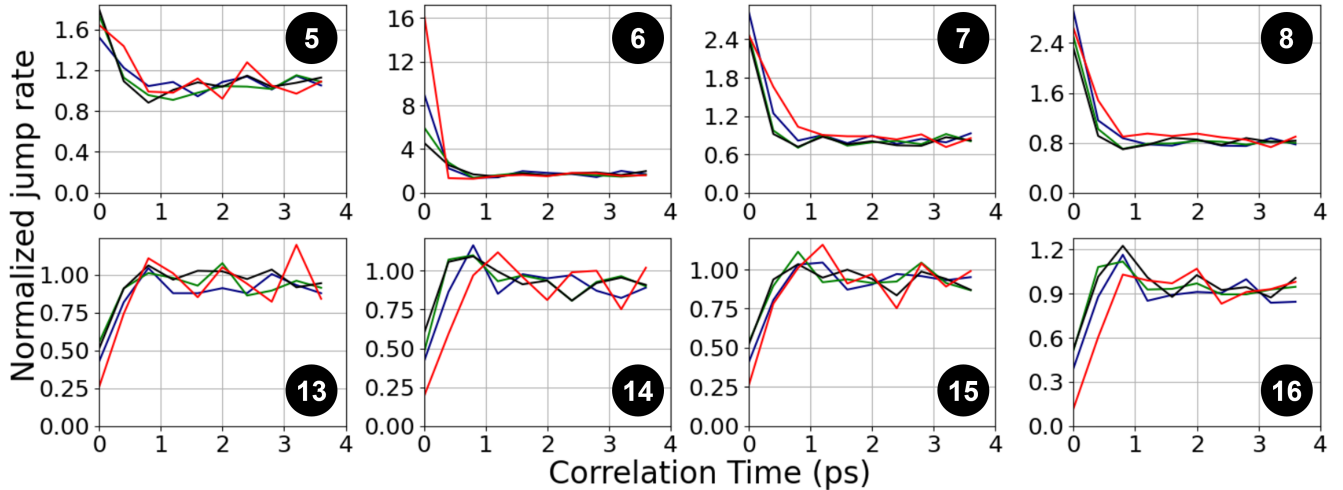


Figure 6 Normalized jumping rate against correlation time for selected Cases for the family of Bi-doped LLZO structures at 1773K. Colors represent different dopant molar contents. [Red = 0, Blue = 0.5, Green = 0.75, Black = 1]. Table 2 describes of the pair correlation cases.

Conclusions

In summary, DFT-MD simulations reveal the mechanisms behind the role of aliovalent doping on ion transport in LLZO. Consistent with experiments, the simulations at $T=1273$ K on $Li_{7-x}La_3Zr_{2-x}M_xO_{12}$ with $M=Ta/Bi$ show an increase in Li diffusion coefficient with doping, up to $x\sim 0.5$ (Li+ concentration of approximately 6.5), followed by a decrease. The mechanisms responsible for the maximum in diffusivity are the main focus of this paper. Analysis of the MD simulations reveals an initial decrease in the occupancy of both octahedral and tetrahedral sites with doping and the consequent reduction in Li+ concentration. Surprisingly, we find a change in this trend, with an increase in the occupancy of the low-energy T sites with decreasing Li+ concentration. This is due to a reduction in the electrostatic repulsion that forces the Li+ to the high-energy O sites in pure LLZO. The maximum in diffusivity originates from the interplay between the increase in vacancy concentration with doping that speeds up transport with the higher occupation of the low-energy T sites that increases the overall activation energy for diffusion. A detailed analysis of the correlations

between different jumps shows the importance of correlated motions and that correlations are seen not just between neighboring sites but also between second nearest neighbors. Our results indicate that increased Li⁺ conductivity would be achieved by reducing the energy difference between the octahedral and tetrahedral sites.

Code and data availability

Scripts for VASP MD simulations and all analysis discussed in this publication are available on Github⁴⁰. A reduced example for a system is also provided there.

Acknowledgements

We acknowledge computational resources from nanoHUB and Purdue University through the Network for Computational Nanotechnology. J. C. V. thanks the Science and Technology Council of Mexico (Consejo Nacional de Ciencia y Tecnología, CONACYT) for its financial support of this research. The authors gratefully acknowledge valuable comments from Dr. Omar Israel Gonzalez-Pena from the Monterrey Institute of Technology and Higher Education.

Ethics declarations

Conflict of interest

On behalf of all authors, the corresponding author states that there is no conflict of interest.

References

- [1] Jian Duan, Xuan Tang, Haifeng Dai, Ying Yang, Wangyan Wu, Xuezhe Wei, and Yunhui Huang. Building safe lithium-ion batteries for electric vehicles: a review. *Electrochemical Energy Reviews*, 3(1):1–42, 2020.
- [2] Xiayue Fan, Bin Liu, Jia Ding, Yida Deng, Xiaopeng Han, Wenbin Hu, and Cheng Zhong. Flexible and wearable power sources for next-generation wearable electronics. *Batteries & Supercaps*, 3(12):1262–1274, 2020.
- [3] Boucar Diouf and Ramchandra Pode. Potential of lithium-ion batteries in renewable energy. *Renewable Energy*, 76:375–380, 2015.
- [4] Lei Fan, Shuya Wei, Siyuan Li, Qi Li, and Yingying Lu. Recent progress of the solid-state electrolytes for high-energy metal-based batteries. *Advanced Energy Materials*, 8(11):1702657, 2018.
- [5] Cong Li, Zhen-yu Wang, Zhen-jiang He, Yun-jiao Li, Jing Mao, Ke-hua Dai, Cheng Yan, and Jun-chao Zheng. An advance review of solid-state battery: Challenges, progress and prospects. *Sustainable Materials and Technologies*, 29:e00297, 2021.

- [6] Ramaswamy Murugan, Venkataraman Thangadurai, and Werner Weppner. Fast lithium ion conduction in garnet-type $\text{Li}_7\text{La}_3\text{Zr}_2\text{O}_{12}$. *Angewandte Chemie International Edition*, 46(41):7778–7781, 2007.
- [7] Alfred Junio Samson, Kyle Hofstetter, Sourav Bag, and Venkataraman Thangadurai. A bird’s-eye view of Li-stuffed garnet-type $\text{Li}_7\text{La}_3\text{Zr}_2\text{O}_{12}$ ceramic electrolytes for advanced all-solid-state Li batteries. *Energy & Environmental Science*, 12(10):2957–2975, 2019.
- [8] Jiantao Han, Jinlong Zhu, Yutao Li, Xiaohui Yu, Shanmin Wang, Gang Wu, Hui Xie, Sven C Vogel, Fujio Izumi, Koichi Momma, et al. Experimental visualization of lithium conduction pathways in garnet-type $\text{Li}_7\text{La}_3\text{Zr}_2\text{O}_{12}$. *Chemical Communications*, 48(79):9840–9842, 2012.
- [9] Lucienne Buannic, Brahim Orayech, Juan-Miguel Lopez Del Amo, Javier Carrasco, Nebil A Katcho, Frederic Aguesse, William Manalastas, Wei Zhang, John Kilner, and Anna Llordes. Dual substitution strategy to enhance Li^+ ionic conductivity in $\text{Li}_7\text{La}_3\text{Zr}_2\text{O}_{12}$ solid electrolyte. *Chemistry of materials*, 29(4):1769–1778, 2017.
- [10] Junji Awaka, Norihito Kijima, Hiroshi Hayakawa, and Junji Akimoto. Synthesis and structure analysis of tetragonal $\text{Li}_7\text{La}_3\text{Zr}_2\text{O}_{12}$ with the garnet-related type structure. *Journal of solid state chemistry*, 182(8):2046–2052, 2009.
- [11] Travis Thompson, Jeff Wolfenstine, Jan L Allen, Michelle Johannes, Ashfia Huq, Isabel N David, and Jeff Sakamoto. Tetragonal vs. cubic phase stability in Al-free Ta doped $\text{Li}_7\text{La}_3\text{Zr}_2\text{O}_{12}$ (LLZO). *Journal of Materials Chemistry A*, 2(33):13431–13436, 2014.
- [12] Alexander G Squires, David O Scanlon, and Benjamin J Morgan. Native defects and their doping response in the lithium solid electrolyte $\text{Li}_7\text{La}_3\text{Zr}_2\text{O}_{12}$. *Chemistry of Materials*, 32(5):1876–1886, 2019.
- [13] Yanhua Zhang, Fei Chen, Junyang Li, Lianmeng Zhang, Jiajun Gu, Di Zhang, Katsuhiko Saito, Qixin Guo, Ping Luo, and Shijie Dong. Regulation mechanism of bottleneck size on Li^+ migration activation energy in garnet-type $\text{Li}_7\text{La}_3\text{Zr}_2\text{O}_{12}$. *Electrochimica Acta*, 261:137–142, 2018.
- [14] Wolfgang G Zeier. Structural limitations for optimizing garnet-type solid electrolytes: a perspective. *Dalton Transactions*, 43(43):16133–16138, 2014.
- [15] Derek K Schwanz, Andres Villa, Mahalingam Balasubramanian, Benjamin Helfrecht, and Ernesto E Marinero. Bi aliovalent substitution in $\text{Li}_7\text{La}_3\text{Zr}_2\text{O}_{12}$ garnets: Structural and ionic conductivity effects. *Aip Advances*, 10(3):035204, 2020.
- [16] Juan C Verduzco, Ernesto E Marinero, and Alejandro Strachan. An active learning approach for the design of doped LLZO ceramic garnets for battery applications. *Integrating Materials and Manufacturing Innovation*, 10(2):299–310, 2021.
- [17] N Bernstein, MD Johannes, and Khang Hoang. Origin of the structural phase transition in $\text{Li}_7\text{La}_3\text{Zr}_2\text{O}_{12}$. *Physical review letters*, 109(20):205702, 2012.
- [18] Katharina Meier, Teodoro Laino, and Alessandro Curioni. Solid-state electrolytes: revealing the mechanisms of Li-ion conduction in tetragonal and cubic LLZO by first-principles calculations. *The Journal of Physical Chemistry C*, 118(13):6668–6679, 2014.

- [19] Randy Jalem, Yoshihiro Yamamoto, Hiromasa Shiiba, Masanobu Nakayama, Hirokazu Munakata, Toshihiro Kasuga, and Kiyoshi Kanamura. Concerted migration mechanism in the Li ion dynamics of garnet-type $\text{Li}_7\text{La}_3\text{Zr}_2\text{O}_{12}$. *Chemistry of Materials*, 25(3):425–430, 2013.
- [20] Lincoln J Miara, Shyue Ping Ong, Yifei Mo, William Davidson Richards, Youngsin Park, Jae-Myung Lee, Hyo Sug Lee, and Gerbrand Ceder. Effect of Rb and Ta doping on the ionic conductivity and stability of the garnet $\text{Li}_{7+2x-y}(\text{La}_{3-x}\text{Rb}_x)(\text{Zr}_{2-y}\text{Ta}_y)\text{O}_{12}$ ($0 \leq x \leq 0.375$, $0 \leq y \leq 1$) superionic conductor: A first principles investigation. *Chemistry of Materials*, 25(15):3048–3055, 2013.
- [21] Randy Jalem, Masanobu Nakayama, William Manalastas Jr, John A Kilner, Robin W Grimes, Toshihiro Kasuga, and Kiyoshi Kanamura. Insights into the lithium-ion conduction mechanism of garnet-type cubic $\text{Li}_5\text{La}_3\text{Ta}_2\text{O}_{12}$ by ab-initio calculations. *The Journal of Physical Chemistry C*, 119(36):20783–20791, 2015.
- [22] Lincoln J Miara, William Davidson Richards, Yan E Wang, and Gerbrand Ceder. First-principles studies on cation dopants and electrolyte—cathode interphases for lithium garnets. *Chemistry of Materials*, 27(11):4040–4047, 2015.
- [23] Chi Chen, Ziheng Lu, and Francesco Ciucci. Data mining of molecular dynamics data reveals li diffusion characteristics in garnet $\text{Li}_7\text{La}_3\text{Zr}_2\text{O}_{12}$. *Scientific reports*, 7(1):1–8, 2017.
- [24] Benjamin J Morgan. Lattice-geometry effects in garnet solid electrolytes: a lattice-gas monte carlo simulation study. *Royal Society open science*, 4(11):170824, 2017.
- [25] G. Kresse and J. Furthmüller. Efficiency of ab-initio total energy calculations for metals and semiconductors using a plane-wave basis set. *Computational Materials Science*, 6(1):15–50, July 1996.
- [26] G. Kresse and J. Furthmüller. Efficient iterative schemes for ab initio total-energy calculations using a plane-wave basis set. *Physical Review B*, 54(16):11169–11186, October 1996. Publisher: American Physical Society.
- [27] John P Perdew, Adrienn Ruzsinszky, Gábor I Csonka, Oleg A Vydrov, Gustavo E Scuseria, Lucian A Constantin, Xiaolan Zhou, and Kieron Burke. Restoring the density-gradient expansion for exchange in solids and surfaces. *Physical review letters*, 100(13):136406, 2008.
- [28] John P. Perdew, Kieron Burke, and Matthias Ernzerhof. Generalized Gradient Approximation Made Simple. *Physical Review Letters*, 77(18):3865–3868, October 1996. Publisher: American Physical Society.
- [29] P. E. Blöchl. Projector augmented-wave method. *Physical Review B*, 50(24):17953–17979, December 1994. Publisher: American Physical Society.
- [30] Yan Chen, Ezhiylmurugan Rangasamy, Chengdu Liang, and Ke An. Origin of high Li^+ conduction in doped $\text{Li}_7\text{La}_3\text{Zr}_2\text{O}_{12}$ garnets. *Chemistry of Materials*, 27(16):5491–5494, 2015. (ICSD 238685).
- [31] G Bergerhoff, ID Brown, and F Allen. Crystallographic databases. *International Union of Crystallography, Chester*, 360:77–95, 1987.

- [32] Reinhard Wagner, Daniel Rettenwander, Gunther J Redhammer, Gerold Tippelt, Gebhard Sabathi, Maurizio E Musso, Bernhard Stanje, Martin Wilkening, Emmanuelle Suard, and Georg Amthauer. Synthesis, crystal structure, and stability of cubic $\text{Li}_{7-x}\text{La}_3\text{Zr}_{2-x}\text{Bi}_x\text{O}_{12}$. *Inorganic chemistry*, 55(23):12211–12219, 2016.
- [33] Alan Logéat, Thomas Köhler, Ulrich Eisele, Barbara Stiaszny, Andreas Harzer, Michael Tovar, Anatoliy Senyshyn, Helmut Ehrenberg, and Boris Kozinsky. From order to disorder: The structure of lithium-conducting garnets $\text{Li}_{7-x}\text{La}_3\text{Ta}_x\text{Zr}_{2-x}\text{O}_{12}$ ($x=0-2$). *Solid State Ionics*, 206:33–38, 2012.
- [34] Yuxing Wang and Wei Lai. High ionic conductivity lithium garnet oxides of $\text{Li}_{7-x}\text{La}_3\text{Zr}_{2-x}\text{Ta}_x\text{O}_{12}$ compositions. *Electrochemical and Solid-State Letters*, 15(5):A68, 2012.
- [35] Yan Wang, William Davidson Richards, Shyue Ping Ong, Lincoln J Miara, Jae Chul Kim, Yifei Mo, and Gerbrand Ceder. Design principles for solid-state lithium superionic conductors. *Nature materials*, 14(10):1026–1031, 2015.
- [36] Xingfeng He, Yizhou Zhu, and Yifei Mo. Origin of fast ion diffusion in super-ionic conductors. *Nature communications*, 8(1):1–7, 2017.
- [37] Stefan Adams and Rayavarapu Prasada Rao. Ion transport and phase transition in $\text{Li}_{7-x}\text{La}_3(\text{Zr}_{2-x}\text{M}_x)\text{O}_{12}$ ($\text{M}=\text{Ta}^{5+}, \text{Nb}^{5+}, x=0, 0.25$). *Journal of Materials Chemistry*, 22(4):1426–1434, 2012.
- [38] Ming Xu, Min Sik Park, Jae Myung Lee, Tae Young Kim, Young Sin Park, and Evan Ma. Mechanisms of Li^+ transport in garnet-type cubic $\text{Li}_{3+x}\text{La}_3\text{M}_2\text{O}_{12}$ ($\text{M}=\text{Te}, \text{Nb}, \text{Zr}$). *Physical Review B*, 85(5):052301, 2012.
- [39] Yuxing Wang, Matthew Klenk, Katharine Page, and Wei Lai. Local structure and dynamics of lithium garnet ionic conductors: a model material $\text{Li}_5\text{La}_3\text{Ta}_2\text{O}_{12}$. *Chemistry of Materials*, 26(19):5613–5624, 2014.
- [40] Juan C. Verduzco and Alejandro Strachan. Atomistic mechanisms underlying the maximum in diffusivity in doped $\text{Li}_7\text{La}_3\text{Zr}_2\text{O}_{12}$. <https://github.itap.purdue.edu/StrachanGroup/doped-llzo-dftmd>. (accessed 2023-05-04).

Supporting Information

Supplementary figures and tables related to the analysis

Supporting Information: Atomistic mechanisms underlying the maximum in diffusivity in doped $\text{Li}_7\text{La}_3\text{Zr}_2\text{O}_{12}$

Juan C. Verduzco, Ernesto E. Marinero, and Alejandro Strachan*

*Corresponding author:

Alejandro Strachan (strachan@purdue.edu)

Phone: +1 765 496 3551

Fax: +1 765 494 1204

School of Materials Engineering and Birck Nanotechnology Center
Purdue University, West Lafayette, Indiana, 47907 USA

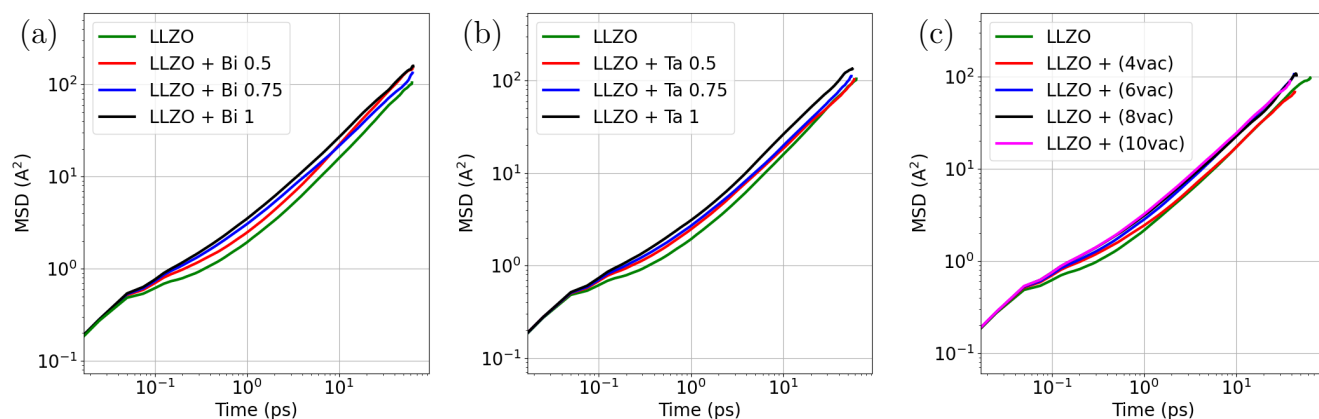


Figure S1 Time average mean square displacement (MSD) for LLZO structures at 1773K, (a) Bi-doped structures, (b) Ta-doped structures, and (c) structures with artificial vacancies.

Table S1 Transitions between tetrahedral and octahedral sites for each system.

STRUCTURE	T \rightarrow O JUMPS (1773K)	O \rightarrow T JUMPS (1773K)	T \rightarrow O JUMPS (1273K)	O \rightarrow T JUMPS (1273K)
LLZO	731	733	475	474
LLZO (Bi = 0.5)	896	900	787	785
LLZO (Bi = 0.75)	1074	1079	792	793
LLZO (Bi = 1)	1179	1187	918	918
LLZO (Ta = 0.5)	850	849	756	753
LLZO (Ta = 0.75)	837	835	803	801
LLZO (Ta = 1)	946	948	790	786
LLZO (LiV = 0.5)	645	639	521	521
LLZO (LiV = 0.75)	669	673	341	337
LLZO (LiV = 1)	768	773	574	575
LLZO (LiV = 1.25)	657	658	504	512

Table S2 Jumping statistics for residence times of doped LLZO garnets.

STRUCTURE	TETRAHEDRAL RES TIME (MEAN) (PS)	TETRAHEDRAL RES TIME (95% CI) (PS)	OCTAHEDRAL RES TIME (MEAN) (PS)	OCTAHEDRAL RES TIME (95% CI) (PS)
LLZO (1773K)	0.930	0.059	3.586	0.231
LLZO (Bi = 0.5) (1773K)	0.683	0.033	2.817	0.176
LLZO (LiV = 0.5)(1773K)	0.669	0.041	2.656	0.182
LLZO (Bi = 0.5) (1273K)	0.828	0.056	3.266	0.238

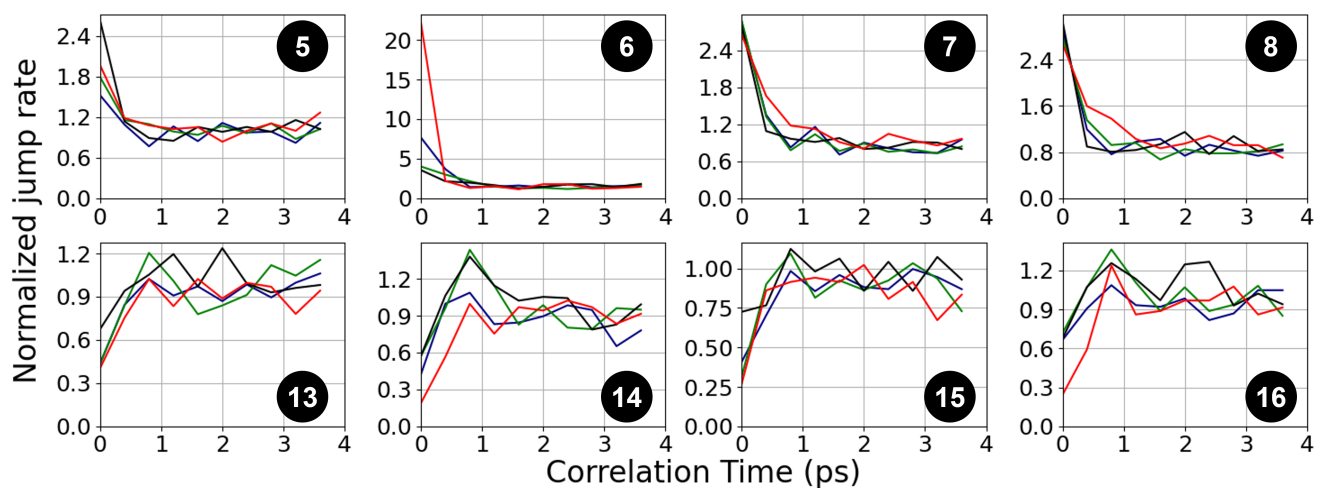


Figure S2 Normalized jumping rate against correlation time for selected mechanisms for the family of Bi-doped LLZO structures at 1273K. Colors represent different dopant contents. [Red = 0, Blue = 0.5, Green = 0.75, Black = 1]. Table 2 describes of the pair correlation cases.

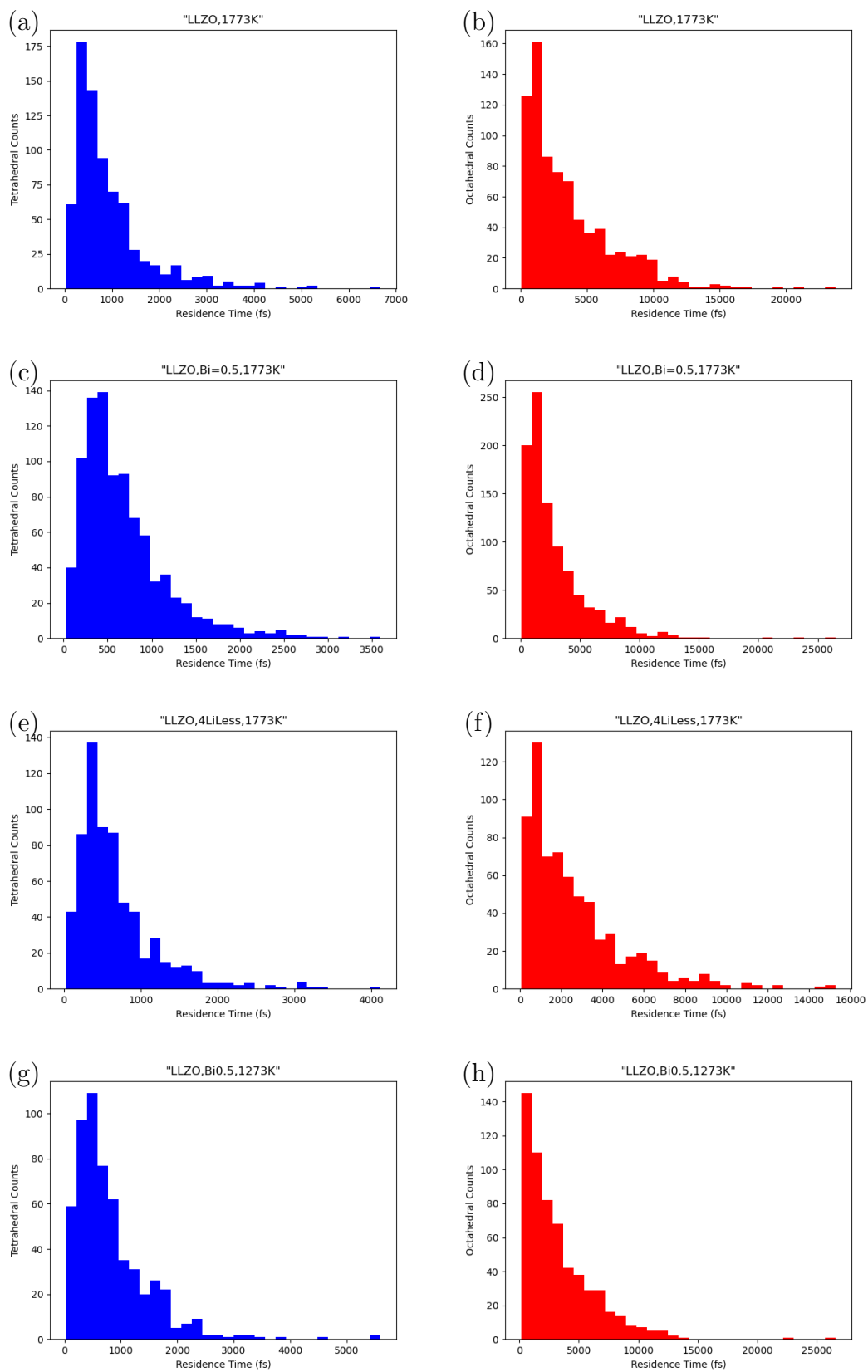


Figure S3 Residence time distributions for (a,b) LLZO (1773K), (c-d) LLZO (Bi = 0.5) (1773K), (e-f) LLZO (LiV = 0.5)(1773K), (g-h) LLZO (Bi = 0.5) (1273K).